Integrated Solar-Driven Device with a Front Surface Semitransparent Catalysts for Unassisted CO$_2$ Reduction

Wen-Hui Cheng, Matthias H. Richter, Ralph Müller, Michael Kelzenberg, Sisir Yalamanchili, Phillip R. Jahelka, Andrea N. Perry, Pin Chieh Wu, Rebecca Saive, Frank Dimroth, Bruce S. Brunschwig,* Thomas Hannappel,* and Harry A. Atwater*

Monolithic integrated photovoltaic-driven electrochemical (PV-EC) artificial photosynthesis is reported for unassisted CO$_2$ reduction. The PV-EC structures employ triple junction photoelectrodes with a front mounted semitransparent catalyst layer as a photocathode. The catalyst layer is comprised of an array of microscale triangular metallic prisms that redirect incoming light toward open areas of the photoelectrode to reduce shadow losses. Full wave electromagnetic simulations of the prism array (PA) structure guide optimization of geometries and length scales. An integrated device is constructed with Ag catalyst prisms covering 35% of the surface area. The experimental device has close to 80% of the transmittance with a catalytic surface area equivalent 144% of the glass substrate area. Experimentally this photocathode demonstrates a direct solar-to-CO conversion efficiency of 5.9% with 50 h stability. Selective electrodeposition of Cu catalysts onto the surface of the Ag triangular prisms allows CO$_2$ conversion to higher value products enabling demonstration of a solar-to-C$_{2+}$ product efficiency of 3.1%. This design featuring structures that have a semitransparent catalyst layer on a PV-EC cell is a general solution to light loss by shadowing for front surface mounted metal catalysts, and opens a route for the development of artificial photosynthesis based on this scalable design approach.

1. Introduction

The use of solar radiation to transform low energy chemicals into high energy products in an integrated monolithic device is an attractive approach for direct solar fuels generation.[1] The conversion of photon energy into chemical bonds facilitates long term storage and transport of solar energy.[2] Integrated solar conversion devices require light absorbers which can provide the necessary photovoltage to overcome the chemical potential differences as well as cathodic and anodic overpotentials for the reactions, e.g., $U > 1.23$ V for H$_2$/O$_2$ or $U > 1.34$ V for CO/O$_2$.[3] Efficient solar-to-fuel conversion requires the use of multijunction semiconductor photovoltaic device structures with suitable bandgap combinations,[4] that capture close to 100% of the solar photon flux. Further, catalysts with low overpotential capable of catalytic currents close to the short circuit current of the multijunction photovoltaic (PV) are required. Thus, a catalyst layer

W.-H. Cheng
Department of Materials Science and Technology
National Cheng Kung University
Tainan 701, Taiwan

W.-H. Cheng, M. Kelzenberg, S. Yalamanchili, P. R. Jahelka, H. A. Atwater
Department of Applied Physics and Material Science
California Institute of Technology
Pasadena, CA 91125, USA
E-mail: haa@caltech.edu

M. H. Richter[+]
Division of Engineering and Applied Science
California Institute of Technology
Pasadena, CA 91125, USA

R. Müller, F. Dimroth
Fraunhofer Institute for Solar Energy Systems ISE
D-79110 Freiburg, Germany

The ORCID identification number(s) for the author(s) of this article can be found under https://doi.org/10.1002/aenm.202201062.

[+]Present address: DeepXscan GmbH, D-01324 Dresden, Germany

A. N. Perry
Department of Physics
Massachusetts Institute of Technology
Cambridge, MA 02139, USA

P. C. Wu
Department of Photonics
National Cheng Kung University
Tainan 70101, Taiwan

R. Saive
Inorganic Materials Science
Mesa+ Institute for Nanotechnology
University of Twente
Enschede, NB 7522, Netherlands

B. S. Brunschwig
Beckman Institute
California Institute of Technology
Pasadena, CA 91125, USA
E-mail: bsb@caltech.edu

T. Hannappel
Department of Physics
Technische Universität Ilmenau
D-98693 Ilmenau, Germany
E-mail: thomas.hannappel@tu-ilmenau.de

ADVANCED
SCIENCE NEWS
www.advancedsciencenews.com

ADVANCED
ENERGY
MATERIALS
www.advenergymat.de

mounted on the front surface of a semiconductor cell must be both catalytically highly active and nearly transparent. In a previous study on solar-to-hydrogen conversion, Rh nanoparticle catalysts were integrated on photocathodes.[5] Minimal parasitic absorption or reflection occurred due to the small size of the nanoparticles (<10 nm), which shifted their plasmonic absorption to the UV.[5] However, this is not a general solution for CO_2 reduction systems.

The complexity of the CO_2 reduction (CO_2R) kinetics requires control of both the competing hydrogen evolution and CO_2 reduction. Further, reaction selectivity is required given the number of possible CO_2R products.[6,7] The relatively low activities of CO_2R catalysts necessitate a high catalytic surface area to achieve catalytic currents that match the solar flux, e.g., short circuit current of the PV, while catalyst opacity can limit the light absorption. Assessments examining integrated device structures for CO_2R have focused on either front side (electrolyte) illuminated photoanodes (anode facing illumination) with dark cathodes,[8,9] or cathodes[10] illuminated from the rear side (nonelectrolyte) with a separate dark anode. Both approaches avoid the challenge of monolithic device integration using a front side illuminated cathode. Other approach utilizing light absorber which also functions as cathodic catalyst, however, is limited by materials selection. Thus, there is a need to develop general strategies for the design and fabrication of integrated device structures using front illuminated cathodes. A literature review of the reported solar driven CO_2 reduction device is included in Table S1 in the Supporting Information.

In earlier demonstrations of Si photocathodes using nonporous metal catalysts, ≈50% of the incident light[11] was blocked or absorbed by the catalyst layer. The blocked radiation no only reduces the photon flux but can complicate the current matching between subcells of a multijunction device due to changes in the illumination spectrum. Thus, minimizing light blocking and/or absorption by catalyst layers is of prime importance. The use of nano- and microscaled wire structures[12–15] or of dielectric nanocone textures that guide the incoming light into the device structure[16] are possible. Neither depends on the properties of the catalytic layer. However, the cost-effective

production of such photonically sophisticated architectures is challenging and the applicable catalytic area remains limited.

Herein, we present a light management approach for CO_2R photocathodes using a semitransparent metal prism array (PA) mounted on top of a multijunction PV cell. The PA consists of metal microscaled triangular prims that redirect the incident light to open areas of the PV-EC cell. Since, the III–V semiconductors used for the multijunction device can facilitate unwanted HER[17] and corrode in high or low pH electrolyte, a transparent passivation/protection layer is incorporated on the semiconductor surface.

As a proof of concept, we have studied a metal PA on insulating glass mounted on a triple junction (3J) semiconductor light absorber, illustrated in **Figure 1**a. The microscaled PA reduced the reflection losses of the catalysts. The top semiconductor layer was connected to the metal PA array via metal shunts that bridged the insulating glass layer on the front and back sides of the electrode, see Figure S1 in the Supporting Information. To catalyze CO_2R, silver (Ag), gold (Au), and copper (Cu) were chosen as the PA metal. The PA can be fabricated on any planar surface. Further, we used two different sets of 3J layer structures as the light absorption layer to measure performance.

2. Results and Discussion

The metal catalyst PA was constructed from Ag triangular prisms with heights and widths of 5 and 2.5 μm, respectively. Spacing between the prisms was ∞, 12.5, 7.1, 5.0 4.0, 3.0 μm with geometric coverages of the semiconductor surfaces of 0%, 20%, 35%, 50%, 63%, and 83%, respectively. With these coverages, the thickness of the metal layer, if uniformly distributed on the surface, would be 0, 500, 875, 1.25, 1.56, and 2.08 μm, respectively. To prevent coupling of the light into the metal grid structure the width of the prisms, w, was made much greater than the wavelength of the incident light.

COMSOL Multiphysics software was used to model the optical response of the structures to the varying metal coverages. Figure 1b–d shows the simulated transmittance,

Figure 1. a) Schematic of triangular Ag metal PA on top of a glass insulating layer on top of a semiconductor photoabsorber. The metal contact on the perimeter of the glass functions as conducting bridge between the catalyst and light absorber. The multicolor arrows show income light redirected toward the semiconductor. Simulated b) transmittance, c) reflectance, and d) absorptance spectra, respectively, of a Ag-PA catalyst array with coverages of 0%, 20%, 35%, 50%, 63%, and 83% on glass substrates (width = 2.5 μm and height = 5 μm).
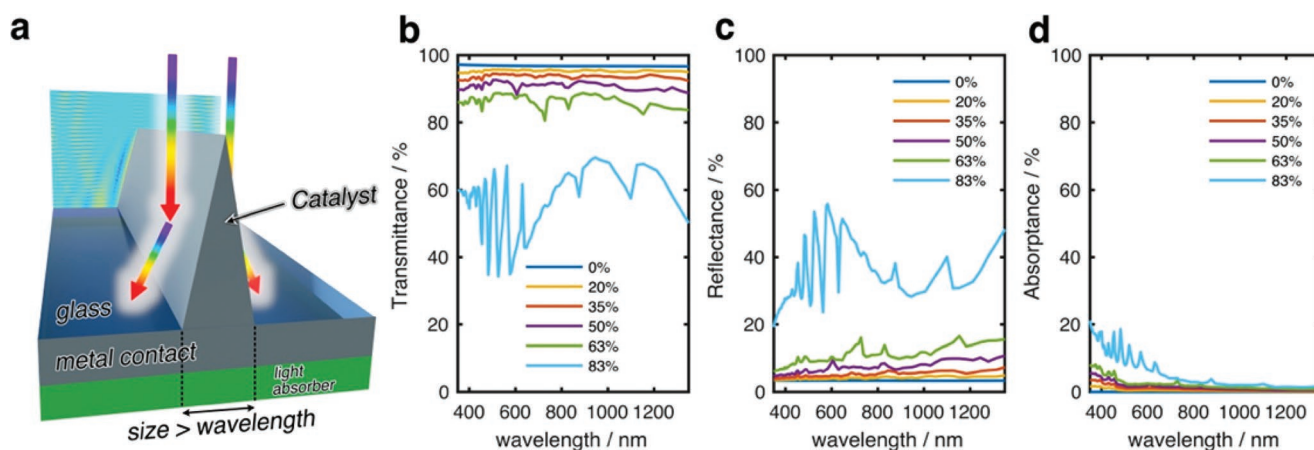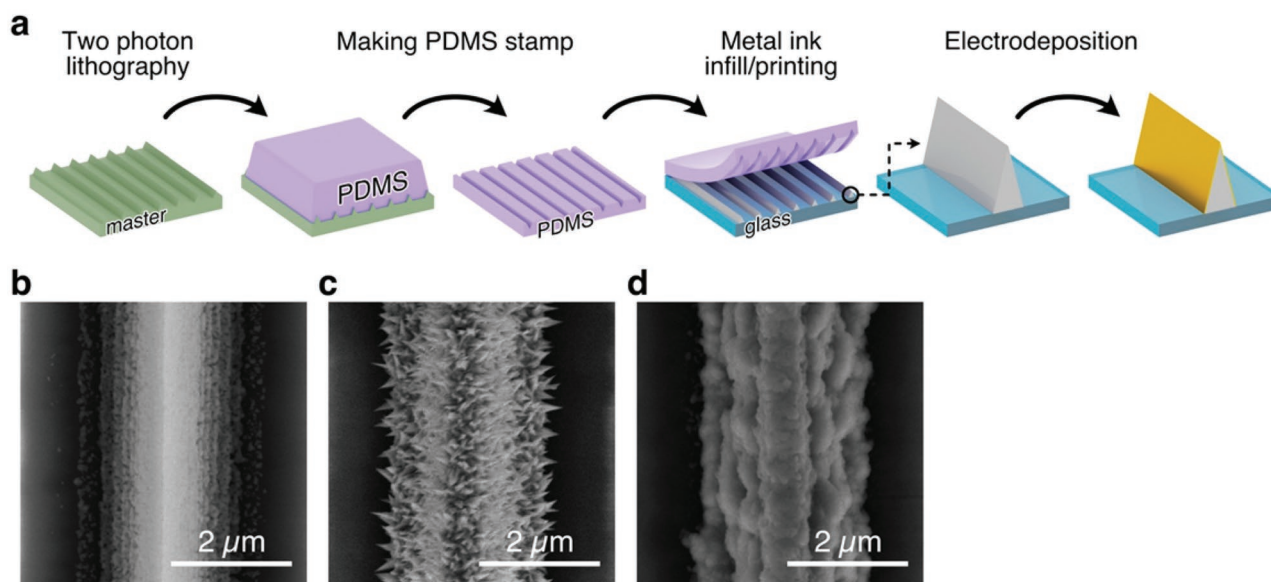
**ADVANCED
SCIENCE NEWS**
www.advancedsciencenews.com

**ADVANCED
ENERGY
MATERIALS**
www.advenergymat.de

Figure 2. a) Illustration of the fabrication process for the arrays of metal catalyst PA; SEM images of b) printed Ag-PA, c) electrodeposited Au on printed Ag-PA, and d) electrodeposited Cu on printed Ag-PA on glass substrate with 35% coverage.

reflectance, and absorptance for Ag catalyst layers for various filling fractions. Increasing the filling fractions increased the catalyst surface area and would reduce overpotential losses. The average reflectance, absorptance, and transmittance for different metal catalyst PAs over the 350–1350 nm range of the incoming light are listed in Table S2 in the Supporting Information. For our calculations, light does not penetrate a Ag layer with a thickness greater than 200 nm (transmittance < 10^{-4}).

The active surface area of PA catalysts can be larger than the total geometric surface area of the underlying light absorber since it is the sum of the upward facing surfaces of the PA. Increases in catalytic surface area would increase the catalytic exchange current and reduce overpotential losses. However, if the increased surface area also increases light blocking by the catalyst layer this would reduce the photocurrent. The catalyst PAs were designed to maximize the solar irradiance reaching the underlying light absorber and not significantly reduce the photocurrent with increasing catalyst coverage. The simulations predicted that a mesoscale Ag-PA that covered of 50% of the PV surface area had a catalyst surface area of >200% of the underlying substrate (or 412% of the covered area) and reflectance/absorptance losses of <10%. Figure S2 (Supporting Information) shows a representation of the simulated electric field profile of a Ag-PA of 35% substrate coverage at λ = 503 nm. The plane wave was reflected from the sides of the metal PA towards the substrate. These results suggest that metal catalyst PA with coverages from 35% to 63% can be utilized as a relatively transparent catalyst layer. We note that the concept of PA assisted incoming light redirection is still valid with incorporation of surface roughness as shown in Figure S3 in the Supporting Information. The roughness average (R_a) obtained by arithmetic mean deviation are 0, 8, 158, and 296 nm accordingly. The size of needles is set be 150 nm of base diameter and 400 nm of height in average.

Ag-PA catalyst arrays with 35% coverage of the light absorber surface were fabricated with a printing process as illustrated in **Figure 2**a. The full details can be found in the methods section.

Briefly, a polymer structure defined with two-photon lithography was used as a master to create a polydimethylsiloxane (PDMS) stamp, followed by metal ink infilling, and annealing to form the final structure. The top view scanning electron microscope (SEM) images of the metal grids is shown in Figure 2b. A 30° tilted SEM image with a cross section of a PA structure, see Figure S4 (Supporting Information), indicates 2.5 µm width and 5 µm height. The catalyst surface area of such a structure is calculated to be 144% of the geometric area and 412% of the covered area. Additionally, layers of Au or Cu have been electrodeposited onto the surface of the printed Ag-PA giving Au/Ag-PA and Cu/Ag-PA structures. The top view SEM images of the two structures are shown in Figure 2c,d. Figure S5a–c in the Supporting Information shows energy-dispersive X-ray spectroscopy (EDX) mappings of the metal catalyst arrays on glass substrates. We observed that after electrodeposition, the Ag catalyst on the PA were conformally covered by the deposited metal (Au or Cu) and EDX signals from Ag are significantly attenuated. The method allows for area-selective deposition of any metal catalyst.

The structure features an insulating glass layer on top of the multijunction PV that passivates the light absorber surface and prevents competing CO_2R or HER reactions thereby improving the solar-to-fuel conversion efficiency. For electrical contact between the top of the PV cell and the metal PA catalyst, a bridging metal shunt was added on two sides of the insulating glass intermediate layer, Figure S1 in the Supporting Information. An alternative configuration of catalysts printed directly on the light absorber would have required the addition of an insulating layer applied only to the PV surface between the PA structures.

Optical transmission, (T) reflection, (R) and absorptance ($1-T-R$) measurements in air for the Ag-PA, Ag/Au-PA, and Ag/Cu-PA structures with 35% PA coverages on glass substrates are shown in **Figure 3**. The glass substrate, blue line in Figure 3, introduced ≈9% reflectance losses from the front

ADVANCED
SCIENCE NEWS

www.advancedsciencenews.com

ADVANCED
ENERGY
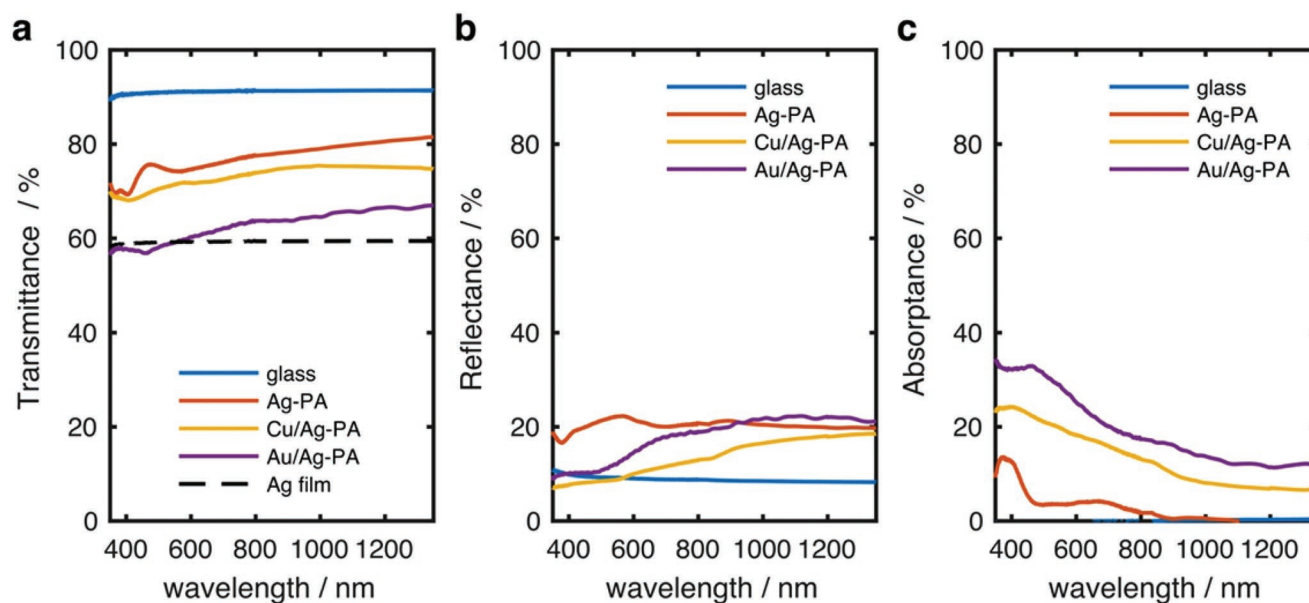MATERIALS

www.advenergymat.de

Figure 3. Experimental results of a) transmittance, b) reflectance spectra, and c) absorptance spectra ($1 - T - R$) spectra, respectively, measured for different metal catalyst PA structures with coverages of 35% on glass substrates. 0% coverage corresponds to the bare glass substrate. A calculated transmission spectrum of a perfectly reflecting Ag film with 35% coverage is included for comparison. ($T_{35\%\_Ag\ film} = T_{glass} \times 65\%$).

and back air/glass interfaces. Simulations of these structures assuming an infinitely thick glass substrate with no reflections from a back glass/air interface are shown in Figure S6 in the Supporting Information. Samples of Ag, Au/Ag, and Cu/Ag-PAs showed reflection loses of from 10% to 20% suggesting that the PAs increased reflection by <11%. However, the experimental transmission was lower than expected from the simulations, Figure S6 in the Supporting Information. The increased losses may be due to the surface roughness of the experimental PA samples as seen in the SEM images in Figure 2b–d. Figure S7 (Supporting Information) for roughened PAs shows increased reflection and absorption comparing to the smooth PAs in Figure S6 in the Supporting Information. Even though rougher surface morphologies are observed for the electrodeposited Cu and Au PAs, these samples did not show higher reflection losses than Ag, Figure S7b in the Supporting Information. Rather, they showed increased absorption, Figure 3c. The needle-like structured morphology of the Ag/Au-PA structure exhibit the highest absorption.

The 35% Ag-PA was the most transparency of the three and showed about 15% better transmittant than the Au/Ag-PA, see Figure 3a. Despite the losses of the 3 structures, their transmission was higher than the transmission expected for a bare glass substrate with 35% of its surface covered by a Ag film of about 60%. The increased transparency of the 35% Ag-PA along with its increased catalyst surface area constitute the crucial benefits of the PA design.

Figure 4 shows three-electrode electrochemical measurements of the three metal PAs in CO_2 saturated 0.1 M $KHCO_3$ (pH of 6.8). For the Ag-PA, the Faradaic efficiency for CO production, f_{CO}, and current density increased with increasing potential with a f_{CO} of 89% at −1.2 V versus RHE (see Figure 4a,d). The comparison of Ag-PA structure and planar structure is shown in Figure S8 in the Supporting Information.

While similar trends in Faradaic efficiency versus applied potential were observed for both samples, the Ag film showed lower current density due to related smaller catalytic surface area. Similar current densities as Ag-PA were observed for both the Au/Ag and Cu/Ag-PAs (Figure 4b,c). For the Au catalysts the optimized f_{CO} was 65% at −0.8 V versus RHE, and for the Cu catalyst it was 90 % for all products other than H_2 at −1.4 V versus RHE. Hydrocarbon products including methane, ethylene, formic acid/formate, acetic acid/acetate, ethanol, and propanol were generated by the Cu/Ag-PA as shown in Figure 4f. Formic acid/formate and acetic acid/acetate are the conjugate acid–base pairs. At −1.4 V versus RHE, seven CO_2 reduction products were detected of which ≈50% were C_{2+} products. Ethanol had the highest Faradaic efficiency of 32%. As expected for a simple Cu surface selectivity was a challenge. We note that a 5 min anodization at 0.02 mA cm^{-2} was applied on Cu. The comparison of catalytic performance with and without anodization is included in Figure S9 in the Supporting Information. The nonanodized sample is inactive for CO_2 reduction with hydrogen as the main product. The surface chemical analysis will be discussed in the later section.

Two-electrode measurements on a full electrochemical cell using the two better performing Ag-PA and Cu/Ag-PA cathodes with a NiO$_x$ foam anode were conducted, **Figure 5**. Characterization details of the activated NiO$_x$ foam anode are shown in Figure S10 in the Supporting Information. The NiO$_x$ anode showed an overpotential of 0.34 V and was stable in CO_2 saturated 0.1 M $KHCO_3$ (pH = 6.8) for >10 h. The Ag-PA cathodes with a NiO$_x$ anode had their highest Faradaic efficiencies for CO production of f_{CO} > 80% at cell voltages of 2.5–2.9 V, Figure 5c. For the Cu/Ag-PA cathodes with NiO$_x$ anodes, Faradaic efficiencies for ethanol production $f_{C_2H_5OH}$ ≈ 30% were achieved with cell voltages ranging from 2.5 to 2.9 V, Figure 5d. Other hydrocarbon products were generated with cell voltages
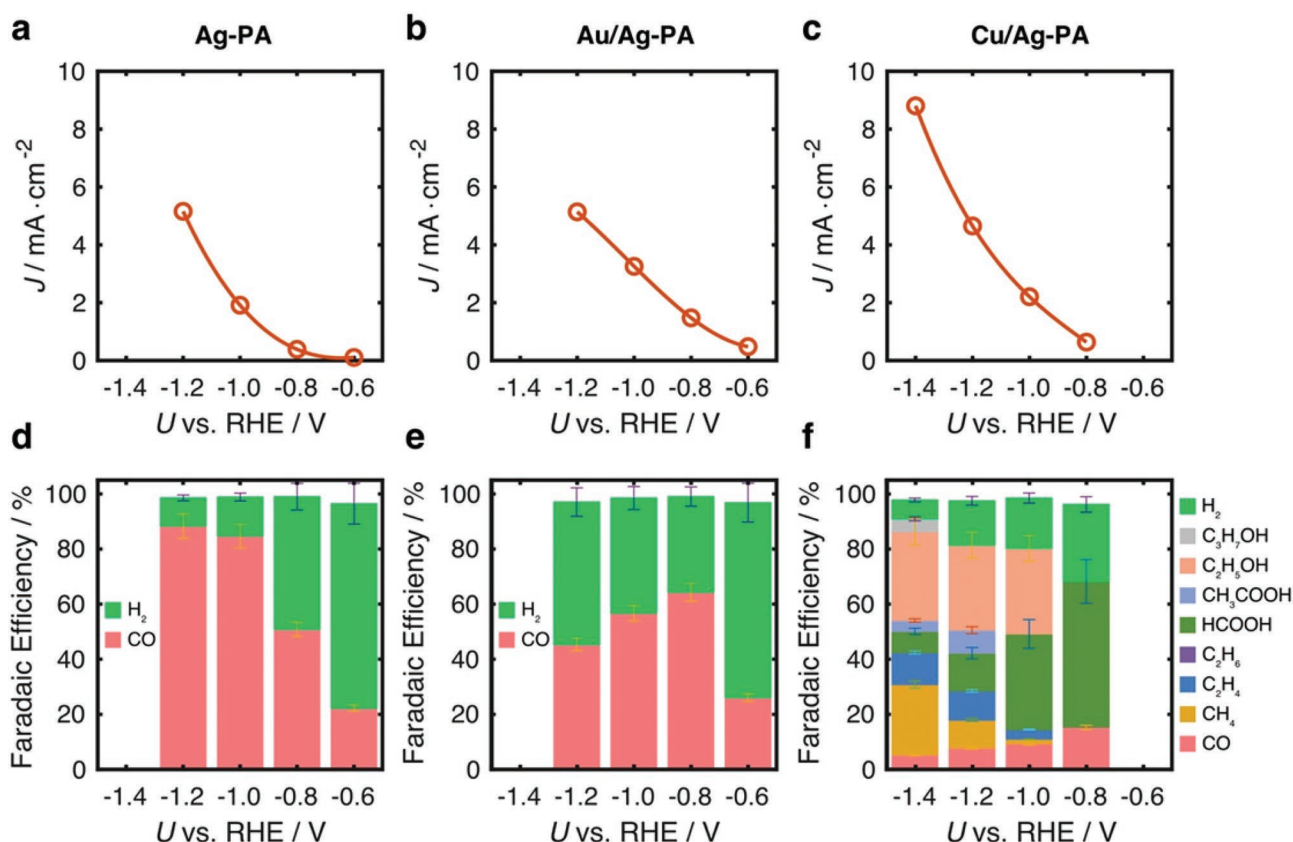
Figure 4. Current density, J, and Faradaic Efficiencies of products versus potentials versus RHE for a,d) Ag b,e) Au/Ag-PA, and c,f) Cu/Ag-PA structures with 35% surface coverage on glass substrates in catalytic process operation (three-electrode measurement).

>2.5 V, with a total CO$_2$R Faradaic efficiency of >80% and a $f_{C_{2+}}$ for C$_{2+}$ products of ≈50% at 2.8 V.

Two 3J-PVs were used one from Spectrolab Inc. with an open circuit voltage of 2.6 V at simulated AM 1.5G and with subcells of GaInP, GaInAs, and Ge (bandgaps E_g of ≈1.82, 1.33, and 0.66 eV, respectively) and another from Fraunhofer Institute for Solar Energy Systems (FhG-ISE) with an open circuit voltage of 3.1 V and subcells of GaInP, GaAs, and Si (E_g ≈ 1.90, 1.43, and 1.12 eV, respectively). Their solid-state J–V characteristics and corresponding solar cell parameters of the bare cells without incorporation of a PA are included in Figure S11 in the Supporting Information.

From the measured transmission spectra of the Ag-PA and Cu/Ag-PA arrays in conjunction with the external quantum efficiencies (EQE) of the two 3J-PV cells, Figure S11 (Supporting Information), the catalysts light blocking effect on each subcell current can be evaluated. The short circuit photocurrent, J_{sc}, of the full cell is limited by the subcell with the lowest $J_{subcell}$. The results are listed in Table S3 in the Supporting Information. For the Spectrolab 3J stack, the middle cell was current limiting, while for the FhG-ISE 3J stack, the bottom cell was current limiting for both the Ag-PA and Cu/Ag-PA. The light limiting current density of the Spectrolab 3J stack decreases from 14.83 to 11.46 mA cm^{-2} for the Ag-PA and to 10.93 mA cm^{-2} for Cu/Ag-PA. Similarly, the light limiting current density of the FhG-ISE 3J stacks decreases from 12.47 to 9.81 mA cm^{-2} for Ag-PA and to 9.35 mA cm^{-2} for Cu/Ag-PA.

Figure 5a,b includes the measured solid-state J–V curves in air of the two PV stacks after integration with a Ag-PA and Cu/Ag-PA, respectively. The light limiting currents for the two PV stacks were close to the values predicted above. The deviation of the J–V especially for the FhG-ISE 3J stack before and after catalyst integration, Figure S11 (Supporting Information) and Figure 5 is mainly due to the mismatch between the noncovered, illuminated area (defined by the catalyst layer) and the total area of the cell.

Figure 5a,b shows the overlay of the two-electrode catalytic J–V measurements for the metal PA cathodes and NiO$_x$ foam anodes with those of the light absorber J–V curves for the solar cells. The intersection of the curves approximately defines the operation condition of the integrated full PA-PV-EC device without external bias. In Figure 5a, the solid-state J–V curve for the Ag-PA covered Spectrolab 3J and catalytic J–V curve intersects at a cell voltage and current density of U_{cell} = 2.56 V and J = 2.65 mA cm^{-2}. Similarly, for an Ag-PA covered FhG-ISE 3J an intersect at U_{cell} = 2.85 V and J = 5.13 mA cm^{-2} is found. In Figure 5b, solid-state J–V curves taken for the Cu/Ag-PA covered Spectrolab 3J and Cu/Ag-PA/NiO$_x$ catalytic system intersects at U_{cell} = 2.56 V and J = 2.60 mA cm^{-2}. The J–V curves taken with Cu/Ag-PA give U_{cell} = 2.80 V and J = 5.97 mA cm^{-2}.

We experimentally evaluated the 35% Ag-PA with integrated Spectrolab 3J without the NiO$_x$ anode using a three-electrode configuration. The experimental setup is shown in Figure S12 in the Supporting Information. J–V characteristics and product
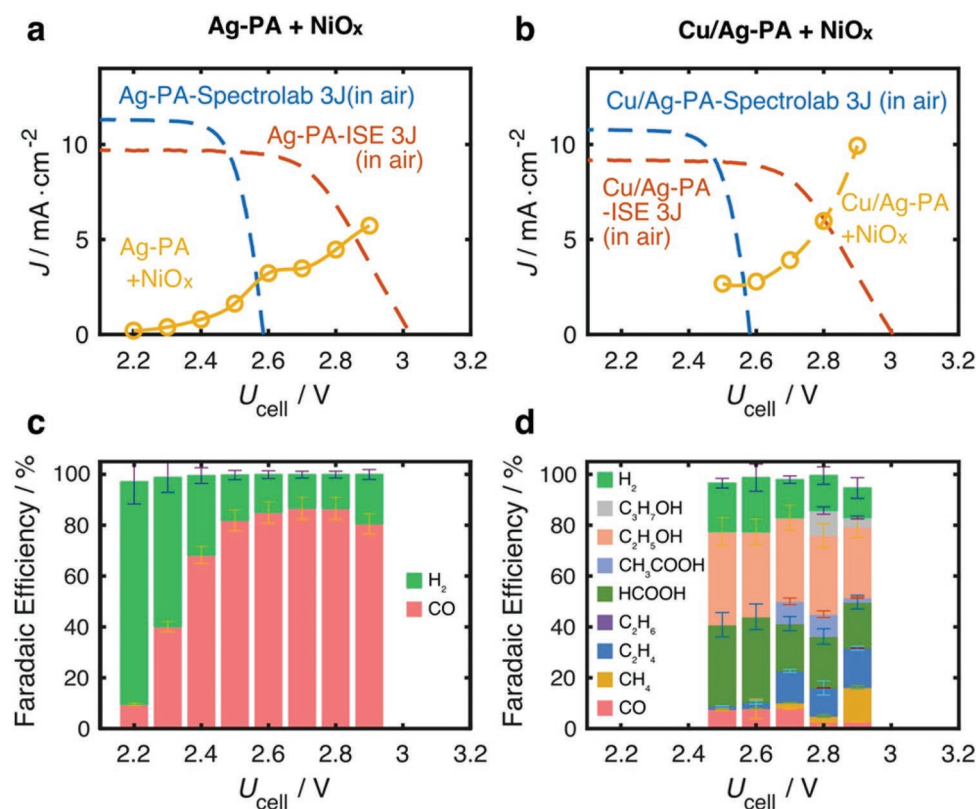
Figure 5. Current density and Faradaic Efficiencies of products as a function of full cell potential for an electrochemical cell using a NiO_x anode and a cathode of a,c) Ag-PA, and b,d) Cu/Ag-PA on glass substrates with 35% coverage. Measurements done using a two-electrode configuration. Measurements of the solid-state $J–V$ curves in air of the Spectrolab 3J and FhG-ISE 3J with catalysts mounted on their front surface as an integrated configuration are included as reference. The intersect between the light absorber $J–V$ curve for the solar cells the and the two-electrode catalytic $J–V$ curves in CO_2 saturated 0.1 M $KHCO_3$ solution shown in (a) and (c) give an approximate operating point for the catalysis cell when running unassisted.

distribution during CO_2R in CO_2 saturated 0.1 M $KHCO_3$ under 1 Sun illuminations are shown in Figure S13 in the Supporting Information. The integrated photoelectrochemical device showed a voltage shift of the $J–V$ curve relative to the Ag-PA electrode without the integrated PV due to the photovoltage of the triple junction photoabsorber of about +2.5 V. Similar trends of product distribution versus applied potentials for the simple and photoactive Ag-PA suggests that the device integration does not introduce notable resistance losses.

Figure 6 shows the results of the unassisted operation of the integrated PA-PV-EC devices with a PA on the 3J PV stack as the photocathodes and NiO_x foam anodes. The operation cell voltage and current density match close to the values predicted in Figure 5a,b. An average solar-to-CO efficiency of 3.0% over 5 h was obtained with the Ag-PA-Spectrolab 3J intergraded device, and 5.4% was realized by integrating the Ag-PA with the FhG-ISE 3J stack. The assessment of solar-to-fuel efficiency calculation is included in Section S1 in the Supporting Information. The Ag-PA catalyst was examined by X-ray photoelectron spectroscopy before and after operation, Figure S14a (Supporting Information) found to be unchanged after 5 h of operation.

In contrast, the Cu catalyst's chemical composition changed after one hour of CO_2R operation, Figure S14b,c in the Supporting Information. The prominent Cu 2p XPS core level

peak at binding energy 932.5 eV corresponds to both Cu^0 and Cu^I species while the little shoulder is due to small amounts of Cu^{II} as CuO (BE: 934.2 eV) and $Cu(OH)_2$ (BE: 935.3 eV).[18] The O 1 s XPS core level spectrum of the pristine sample had three components, with the major contribution from CuO_x (BE: 530.5 eV) and minor shoulders for $Cu(OH)_2$ (BE: 531.6 eV), and an oxygen defect species (BE: 532.5 eV).[18,19] Comparing the before and after CO_2R XPS spectra indicates that while most of the Cu remained in the Cu^0 state there were small changes in the other species. The O 1 s spectra shows that the $Cu(OH)_2$ decreased after 1 h of CO_2R operation. We found that a 5 min anodization of the pristine sample at 0.02 mA cm^{-2} decreased the oxygen defect species and increased the $Cu(OH)_2$ species. Therefore, to maintain the same catalyst composition and avoid any changes in performance due to catalyst decomposition during testing, the Cu electrode was reanodized each hour during its operation. The energy input from anodization was not included in the efficiency calculation.

The Cu/Ag-PA-Spectrolab 3J photocathode coupled with the NiO_x anode exhibited an average total solar-to-fuels efficiency from CO_2R of 2.7% and solar-to-C_{2+} efficiency of 1.1%. The Cu/Ag-PA-FhG-ISE 3J with NiO_x anode gave 5.0% for average total solar-to-fuels efficiency from CO_2R and 3.1% for solar-to-C_{2+} efficiency. These results match closely with those predicted from the measurement of the individual

**ADVANCED
SCIENCE NEWS**

www.advancedsciencenews.com

**ADVANCED
ENERGY
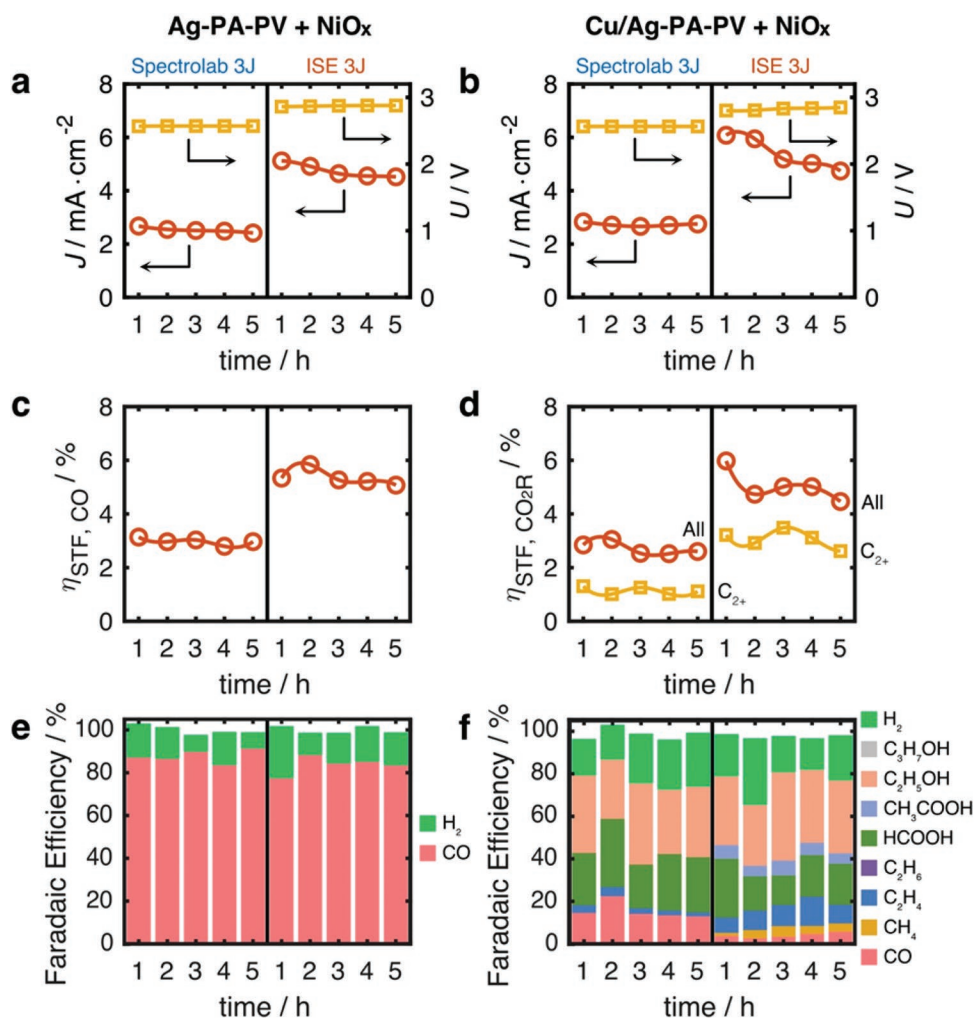MATERIALS**

www.advenergymat.de

Figure 6. Unassisted two-electrode measurements of the integrated PA-PV-EC devices at 0 V versus NiO_x counter electrode under 1 sun illumination (simulated AM 1.5G). a) Current density and cell potential, c) solar-to-CO efficiency, e) Faradaic Efficiency of products with Spectrolab or FhG-ISE 3J-PV stack using a Ag-PA structures with 35% coverage over 5 h operation. b) Current density and cell potential, d) solar-to-fuels efficiency from CO_2R and solar-to-C_{2+} efficiency, f) Faradaic Efficiency of products of device structures with Spectrolab 3J or FhG-ISE 3J-PV stack using a Cu/Ag-PAs with 35% coverage over 5 h operation.
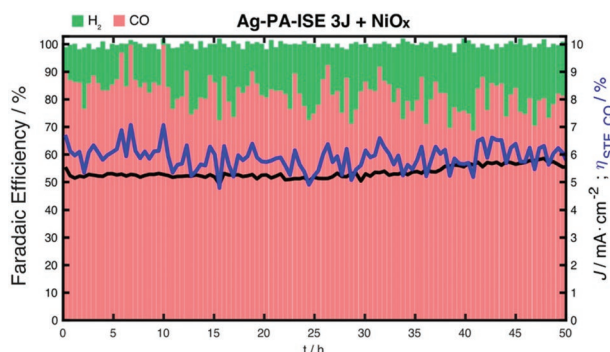
Figure 7. Efficiency and stability assessment of the integrated PA-PV-EC devices composed of Ag-PA arrays on acrylic with 35% catalyst surface coverage and a FhG-ISE 3J stack with NiO_x foam anode without external bias for 50 h operation under 1 sun illumination.

pieces above, demonstrating the highest values for unassisted CO_2R for an integrated monolithic device structure in a two-electrode setup without external bias. The use of metal catalyst PAs with coverages higher than 35% and reduction of the electrical losses due to the mismatch between the light absorber and the printed catalysts would increase the efficiency of the device.

We have printed the Ag-PA arrays on a thin acrylic plate to further improve the adhesion between the metal catalysts and the substrate. We have demonstrated that under unassisted CO_2R the Ag-PA-FhG-ISE 3J cell with NiO_x was stable for over 50 h, **Figure 7**. Here, an average solar-to-CO conversion efficiency of 5.9% was achieved without visible degradation over 50 h. The long-term stability is another essential factor supporting our proof of concept design as a promising solution for integrated PA-PV-EC device.

3. Conclusions

An integrated solar-driven photoelectrochemical device capable of reducing CO_2 in unassisted operation (without externally applied bias) was achieved with 5.9% solar-to-CO efficiency and stability of 50 h using Ag-PA catalysts design mounted on an advanced triple junction (3J) photoabsorber structures. A total solar-to-fuels conversion efficiency from CO_2R of 5.0% and solar-to-C_{2+} efficiency 3.1% with Cu/Ag-PA catalyst structures are realized. The PA catalyst strategy provides a general design for a monolithic front illuminated photocathode device with record solar-to-fuel efficiencies for production CO or for higher value products. Our designs feature structures with a semitransparent catalyst layer mounted on a photocathode that allowed a high solar flux to reach the PV-EC cells. Other metal catalysts can be used to drive different chemical reactions. The approach is not limited to specific combination of semiconductor and metal, and in principle is scalable. Large area printing tool is under development by companies and the electroplating technique to generate different catalytic surfaces is also well known to be extensible. The demonstration of these fabrication processes with make an important advance in the field of solar fuel.

4. Experimental Section

All simulated spectra, including reflectance (R), transmittance (T), absorptance ($\mathbb{A}$), and field distributions were generated by solving Maxwell equations based on the finite element method (FEM) with commercial COMSOL Multiphysics software. The PA metal prism grids were modelled using 2D simulations with periodic boundary conditions at the left and right edges, and infinite boundary conditions were rendered as perfectly matched layers (PMLs) along top and bottom edge, as shown in Figure S2 in the Supporting Information. The geometry parameters that were used in our simulations includes width (w), height (h), pitch (p). Coverage is defined as width (w) divided by pitch (p). A plane-wave source incident from the top in the wavelength range from 350 to 1350 nm was utilized. Spectra for unpolarized light were obtained by averaging the spectra for the two orthogonal polarizations. All materials refractive indices were modeled using tabulated data provided in the software.

Triple junction cells from Spectrolab Inc. (C4MJ) of GaInP/GaInAs/Ge and from the Fraunhofer Institute for Solar Energy Systems, FhG-ISE, of GaInP/GaAs/Si were used in this study. An Oriel Instruments 75 W Solar Simulator was used for simulated AM 1.5G illumination. The corresponding subcell currents with integration of EQE determined the expected short circuit current density under simulated AM 1.5G illumination. The light intensity of the solar simulator was set to provide the expected short circuit current density from the specific triple junction cell. Since the solar irradiance of the solar simulator and a AM 1.5G were not identical in the 800–1000 and 1150–1800 nm regions, the obtained simulated solar irradiance is not expected to be 100 mW cm^{-2}. Nevertheless, it is adequate to represent the performance of a 3J PV cell operation under actual AM 1.5G sunlight.

The fabrication processes of the metal catalyst PA arrays on glass (Schott D-263 M borosilicate coverslip, Thorlabs cover glass) or acrylic are illustrated in Figure 2a. First, a positive PA master was fabricated on a Si substrate using a two-photon lithography technique. Second, a negative PDMS stamp was formed from the lithography master. After a precleaning process of the glass substrate the PDMS stamp was placed onto a glass substrate (structure facing down). Drops of metal ink were placed on the opposing sides (PA exposed) of the stamp. The ink filled the structure via capillary force. The metal grid structures were

then annealed on a hot plate at $\approx$100 °C for 10 min to remove solvent before, the PDMS stamp was peeled away. The PA grids on glass were then re-annealed at 200 °C for 1 h in a muffle furnace in air. SEM images show the metal grids with a cross section of a PA structure, see Figure S4 in the Supporting Information. For Au and Cu PAs additional metal catalysts was electrodeposited in an aqueous solution at 0.1 mA for 2–4 min.

A Cary 5000 UV/vis/NIR with integrating sphere was used to measure reflectance (R), and transmittance (T) spectra of PAs on glass in air. Absorptance spectra of PAs on glass were then calculated by Absorptance = $1 - T - R$. The integrated PA-PV device was made by assembling the PA on glass on top of the triple junction light absorber with the top semiconductor layer connected to the metallized PA array via a metal contact on the perimeter of the electrode that bridged the insulating glass layer, see Figure S1 in the Supporting Information.

A modified polyetheretherketone (PEEK) compression cell (shown in Figure S12 in the Supporting Information) with a lateral off-set between cathode and anode to allow illumination of the cathode was used to the measurement (photo)electrochemical properties of the PA as a photo or electrical cathode. The anode and cathode chambers had volumes of 2 and 4 mL, respectively. The anode and cathode electrode working areas were 6 and 0.2 cm^2, and the membrane area was 1 cm^2. The activated NiO$_x$ foam anode size was enlarged to reduce the overpotential from oxygen evolution reaction (OER) and was folded to fit behind the geometric area of the cathode. A 100×10^{-3} M potassium bicarbonate (KHCO$_3$) saturated with CO_2 was used as the electrolyte for experiments at pH 6.8. The anion exchange membrane (AEM) was chosen as Fumasep FAA-3-50 for lower resistance. A leakless Ag/AgCl reference electrode (0.197 V vs NHE in saturated KCl solution) was used to determine the electrode potential versus RHE in three-electrode experiments. All the electrochemical measurements were conducted using a Biologic VSP-300 potentiostat with scan rates of 50 mV s^{-1}. For unassisted two-electrode measurements, the cell voltage was recorded with a Keithley 2000 multimeter.

The electrochemical product analysis was performed in a continuous flow mode. Humidified carbon dioxide was supplied to the electrochemical cell with flow rates controlled by an Alicat flow controller. The exhaust gases went through a mixing volume followed by an Alicat flow meter, and then to a gas chromatograph (SRI-8610) equipped with a Hayesep D column and a Molsieve 5A column with N$_2$ carrier gas. The gaseous products were analyzed by a thermal conductivity detector (TCD) and a flame ionization detector (FID) equipped with a methanizer. A high-performance liquid chromatograph (HPLC) was used to detect liquid products after 1 h accumulation at each operation condition. Both anolyte and catholyte were sampled to capture possible product crossovers. Quantitative analysis of gaseous and liquid products was based on calibration with several standards over many orders of magnitude in concentration.

Conflict of Interest

The authors declare no conflict of interest.

Data Availability Statement

The data that support the findings of this study are available from the corresponding author upon reasonable request.

Keywords

[1] M. R. Shaner, H. A. Atwater, N. S. Lewis, E. W. McFarland, *Energy Environ. Sci.* **2016**, *9*, 2354.

[2] H. L. Tuller, *Mater. Renew. Sustain. Energy* **2017**, *6*, 3.

[3] M. R. Singh, E. L. Clark, A. T. Bell, *Phys. Chem. Chem. Phys.* **2015**, *17*, 18924.

[4] M. M. May, D. Lackner, J. Ohlmann, F. Dimroth, R. van de Krol, T. Hannappel, K. Schwarzburg, *Sustainable Energy Fuels* **2017**, *1*, 492.

[5] W.-H. Cheng, M. H. Richter, M. M. May, J. Ohlmann, D. Lackner, F. Dimroth, T. Hannappel, H. A. Atwater, H.-J. Lewerenz, *ACS Energy Lett.* **2018**, *3*, 1795.

[6] M. B. Ross, P. De Luna, Y. Li, C. T. Dinh, D. Kim, P. Yang, E. H. Sargent, *Nat. Catal.* **2019**, *2*, 648.

[7] L. Fan, C. Xia, F. Yang, J. Wang, H. Wang, Y. Lu, *Sci. Adv.* **2020**, *6*, eaay3111.

[8] X. Zhou, R. Liu, K. Sun, Y. Chen, E. Verlage, S. A. Francis, N. S. Lewis, C. Xiang, *ACS Energy Lett.* **2016**, *1*, 764.

[9] T. Arai, S. Sato, T. Morikawa, *Energy Environ. Sci.* **2015**, *8*, 1998.

[10] Gurudayal, J. W. Beeman, J. Bullock, H. Wang, J. Eichhorn, C. Towle, A. Javey, F. M. Toma, N. Mathews, J. W. AgerIII, *Energy Environ. Sci.* **2019**, *12*, 1068.

[11] J. T. Song, H. Ryoo, M. Cho, J. Kim, J.-G. Kim, S.-Y. Chung, J. Oh, *Adv. Energy Mater.* **2017**, *7*, 1601103.

[12] Y. Chen, C. W. Li, M. W. Kanan, *J. Am. Chem. Soc.* **2012**, *134*, 19969.

[13] Q. Kong, D. Kim, C. Liu, Y. Yu, Y. Su, Y. Li, P. Yang, *Nano Lett.* **2016**, *16*, 5675.

[14] P. A. Kempler, M. H. Richter, W.-H. Cheng, B. S. Brunschwig, N. S. Lewis, *ACS Energy Lett.* **2020**, *5*, 2528.

[15] S. K. Choi, U. Kang, S. Lee, D. J. Ham, S. M. Ji, H. Park, *Adv. Energy Mater.* **2014**, *4*, 1301614.

[16] S. Yalamanchili, E. Verlage, W.-H. Cheng, K. T. Fountaine, P. R. Jahelka, P. A. Kempler, R. Saive, N. S. Lewis, H. A. Atwater, *Nano Lett.* **2019**, *20*, 502.

[17] H. Lim, J. L. Young, J. F. Geisz, D. J. Friedman, T. G. Deutsch, J. Yoon, *Nat. Commun.* **2019**, *10*, 3388.

[18] B. V. Crist, *Handbook of Monochromatic XPS Spectra: the Elements of Native Oxides*, Wiley, Chichester, England, **2000**.

[19] Q. Zhu, X. Sun, D. Yang, J. Ma, X. Kang, L. Zheng, J. Zhang, Z. Wu, B. Han, *Nat. Commun.* **2019**, *10*, 3851.